

Estimation of Optimal Fiducial Target Registration Error in the Presence of Heteroscedastic Noise

Burton Ma*, Mehdi H. Moghari, Randy E. Ellis, and Purang Abolmaesumi

Abstract—We study the effect of point dependent (heteroscedastic) and identically distributed anisotropic fiducial localization noise on fiducial target registration error (TRE). We derive an analytic expression, based on the concept of mechanism spatial stiffness, for predicting TRE. The accuracy of the predicted TRE is compared to simulated values where the optimal registration transformation is computed using the heteroscedastic errors in variables algorithm. The predicted values are shown to be contained by the 95% confidence intervals of the root mean square TRE obtained from the simulations.

Index Terms—Heteroscedastic noise, image-guided surgery, point-based registration, registration error.

I. INTRODUCTION

FINDING the rigid transformation that best matches one point set to another when the point-to-point correspondences are known is a problem that has been encountered in many fields of research. The problem is most commonly referred to as the fiducial registration problem in computer-aided surgery. Least-squares solutions, for either the rotational component or the complete rigid transformation, have been proposed by numerous authors; [1] and [2] contain discussions of the history of solutions to the problem. Two solutions commonly cited in the medical computing literature are the singular value decomposition method of Arun, Huang, and Blostein [3] and the unit quaternion method of Horn [4]. The use of least-squares assumes that one set of points is noise free and the other set of points is contaminated with independent, identically distributed (iid), isotropic, zero-mean Gaussian noise.

One application of fiducial registration in computer-aided surgery is the measurement of coordinate systems defined by optically tracked reference frames. Optical tracking systems that measure the spatial location of points of infrared light are commonly used in commercial navigated surgical systems. These systems measure coordinate reference frames (CRFs), which are essentially a set of infrared emitting or reflecting

fiducial markers, that are rigidly attached to the tracked object. In some tracking systems, the measurement precision is worse in the viewing direction of the cameras; hence, the noise in the measured point locations is anisotropic. Khadem *et al.* [5] analyzed the jitter for several configurations of optical trackers; jitter was defined as the standard deviation of repeated measurements of the location of a stationary CRF. They found that the jitter was anisotropic with the greatest deviation occurring in the viewing direction of the tracking system. Their results showed an anisotropy as large as a factor of five or more when using a Polaris tracking system with a passive target.

Ohta and Kanatani [6] described an algorithm designed to accommodate point dependent (heteroscedastic) Gaussian noise in both the model and measurement coordinate systems. Their algorithm produced the optimal estimate of rotation using a quaternion renormalization technique, and it required that the noise covariances be specified to within a scalar factor. They defined a covariance matrix for the axis-angle parameterization of rotation, derived its lower bound, and showed that their algorithm was optimal in the sense that it achieved the lower bound. Their quaternion renormalization algorithm had smaller registration errors compared to a conventional least-squares algorithm.

Matei [7] and Matei and Meer [8] described an algorithm that produced optimal estimates of rotation and translation under heteroscedastic noise. Their algorithm solved the heteroscedastic, multivariate errors-in-variables (HEIV) regression problem corresponding to fiducial registration. Estimation of the noise covariance matrices of the two point sets and the confidence intervals were obtained using bootstrap techniques. Their HEIV algorithm had smaller registration errors compared to Ohta and Kanatani's method in their experiments.

Pennec and Thirion [9] used an extended Kalman filter (EKF) as part of a framework for registration using points and frames. Their approach accommodated anisotropic noise in both sets of points to be registered.

Moghari and Abolmaesumi [10] used the unscented Kalman filter (UKF) to solve the fiducial registration problem and estimate the covariance of the state parameters $[t_x, t_y, t_z, \theta_x, \theta_y, \theta_z]^T$, where $[t_x, t_y, t_z]^T$ was the translation and $[\theta_x, \theta_y, \theta_z]^T$ was the vector of Euler angles. Given a sufficient number of markers, their algorithm was able to estimate the mean squared TRE and the distribution of TRE. Their work appears to be an improvement over the EKF algorithm [9] with regard to estimating TRE and its distribution [11].

Dorst [12] analyzed how noise in the measured registration points affected the computed registration parameters. He derived the covariance matrices for the estimated rotational and

Manuscript received April 13, 2009; revised September 23, 2009; accepted September 28, 2009. Current version published March 03, 2010. *Asterisk indicates corresponding author.*

*B. Ma is with the Department of Computing Science and Engineering, York University, Toronto, ON M3J 1P3, Canada (e-mail: burton@cse.yorku.ca).

M. H. Moghari is with the Harvard Medical School, Boston, MA 02115 USA (e-mail: mhedjazi@bidmc.harvard.edu).

R. E. Ellis is with the School of Computing, Queen's University, Kingston, ON K7L 3N6, Canada (e-mail: purang.ellis@cs.queensu.ca).

P. Abolmaesumi is with the Department of Electrical and Computer Engineering, The University of British Columbia, Vancouver, BC V6T 1Z4, Canada (e-mail: purang@ece.ubc.ca).

Digital Object Identifier 10.1109/TMI.2009.2034296

translational parameters given the noise covariances of the two point sets to be registered; the derivation assumed identically distributed noise.

Fitzpatrick *et al.* [2] derived an expression for expected fiducial target registration error (TRE) in k -dimensions. Target registration error is simply the magnitude $\|\mathbf{r} - \mathbf{r}'\|$ where \mathbf{r} is the expected location of a target point and \mathbf{r}' is the registered location the target point. Their statistical derivation was performed assuming that the fiducial localization error (FLE) was accurately modeled by a zero-mean, isotropic, iid Gaussian random variable; Fitzpatrick and West [13] later derived the distribution of TRE under the same noise model. The work by Wiles *et al.* [14] produced expressions for the expected mean, covariance, and rms of TRE under anisotropic FLE conditions assuming a least-squares solution to the registration problem. The assumption of a least-squares solution implied that the registration transformation could be expressed as a singular value decomposition that made possible their statistical derivation. Most recently, using maximum likelihood estimation, Moghari and Abolmaesumi [15] introduced a new solution that provides an estimate for the distribution of TRE under nonidentical anisotropic FLE conditions.

West and Maurer [16] applied their previous results [2], [13] to design targets for optically tracked surgical instruments. They studied primarily planar CRF configurations, although they briefly discussed some of the expected effects of using nonplanar CRFs. It was shown that the expected TRE could be computed by summing in quadrature the individual TREs when there is a composition of transformations (for instance, when one CRF is measured relative to a second CRF).

A method for online estimation of TRE covariance has been described in [17] and [18] that was an extension of the method described by Hoff and Vincent [19]. Given an estimate of the covariances of the feature detection error on the image plane of each tracking camera, the covariances were propagated to produce the covariances of the FLE for each fiducial marker. The FLE covariances were then propagated to produce the covariance of the CRF pose, which was then propagated to produce the TRE covariance. Covariance propagation was performed by linearizing the measurement functions at each step of the propagation.

We have attempted to estimate TRE by modeling the registration problem as an elastic mechanism where the mechanism (the registration points) is suspended by linear springs. The small displacement behavior of an elastic mechanism is governed by the concept of spatial stiffnesses, which has been extensively studied in the fields of robotics and mechanics. Our first attempt at applying a spatial stiffness analysis to a registration problem led to an estimate of an upper bound on TRE for fiducial registration under isotropic iid Gaussian fiducial localization noise [20]. In a second conference paper, we derived the spatial stiffness matrix for surface-based registration under isotropic iid Gaussian point localization noise, and derived heuristics for optimizing registration point selection [21]; an extended version appeared as a journal paper [22]. In a third conference paper, we presented expressions for TRE for both fiducial and surface-based registration under isotropic iid Gaussian noise conditions [23]; the expression for fiducial TRE was identical to that

published by [2]. It can be shown that the stiffness matrices we derived were based on first-order Taylor series approximations of rotation and translation [24]. In a fourth conference paper, we presented an expression for fiducial TRE under anisotropic iid Gaussian noise [25].

We present three significant contributions in this paper. The first contribution is a review of the aspects of mechanism spatial-stiffness, that are relevant to our purposes, from the fields of robotics and mechanics. The second contribution is the derivation of an equation that predicts the expected root mean square TRE (TRE_{rms}) for fiducial registration with heteroscedastic noise assuming an optimal (that is, not least-squares) registration algorithm. The third contribution is a comparison of the predicted TRE_{rms} and simulated values obtained using a least-squares registration algorithm (Horn's method [4]) and the HEIV algorithm. Our simulations show that our equation reliably predicts TRE_{rms} under the assumed noise conditions when the HEIV algorithm is used. We also contribute simulation results comparing the behavior of TRE_{rms} using HEIV algorithm and Horn's algorithm.

II. SPATIAL-STIFFNESS OF A PASSIVE MECHANISM

A common problem in mechanics is determining the relationship between the displacement of a mechanism and the reaction forces that arise. For small displacements about an equilibrium configuration, this *stiffness* relationship is often assumed to be linear and, therefore, is characterized by a spatial-stiffness matrix. This section is a review of the literature discussing the structure and analysis of stiffness matrices. We first provide some mathematical background before proceeding to the literature review. The mathematical notation we use is generally consistent with that of [26] and [27].

A. Screws, Twists, and Wrenches

A rigid transformation of an object is one that preserves both distances and angles; it comprises a rotation and translation. A screw transformation is one representation of a rigid transformation, consisting of a rotation about an axis followed by a translation parallel to the same axis. It is characterized by its axis, magnitude, and pitch.

- The screw axis \mathbf{l} is defined by a point \mathbf{q} and a unit vector \mathbf{w} ; \mathbf{q} is a point on the axis and \mathbf{w} is the direction of the axis. If there is no rotation then the screw represents a pure translation and \mathbf{q} is taken to be the origin.
- The magnitude M of a screw is the amount of rotation, measured in radians, that occurs about the axis. For a pure translation M is taken to be the magnitude of the translation.
- The pitch h of a screw is the ratio of translation distance to rotation angle. A zero pitch screw represents a pure rotation. A pure translation is a screw with $h = \infty$.

A twist is the linear and angular velocity of a rigid body about an instantaneous screw axis. It is a 6-vector $\mathbf{t} = [\mathbf{v}^T \boldsymbol{\omega}^T]^T$ where $\mathbf{v}^T = [v_x \ v_y \ v_z]$ is linear velocity and $\boldsymbol{\omega}^T = [\omega_x \ \omega_y \ \omega_z]$ is rotational velocity. A twist is often used to represent a small displacement rather than velocity, in which case \mathbf{v} is linear translation and $\boldsymbol{\omega}$ is rotation. The screw representation of a twist is axis

$$\begin{aligned} \mathbf{q} &= \frac{\boldsymbol{\omega} \times \mathbf{v}}{\boldsymbol{\omega}^T \boldsymbol{\omega}} \quad \mathbf{w} = \boldsymbol{\omega} \text{ if } \boldsymbol{\omega} \neq \mathbf{0} \\ \mathbf{q} &= \mathbf{0} \quad \mathbf{w} = \mathbf{v} \text{ if } \boldsymbol{\omega} = \mathbf{0}. \end{aligned} \quad (1)$$

magnitude

$$\begin{aligned} M &= \|\boldsymbol{\omega}\| \text{ if } \boldsymbol{\omega} \neq \mathbf{0} \\ M &= \|\mathbf{v}\| \text{ if } \boldsymbol{\omega} = \mathbf{0} \end{aligned} \quad (2)$$

pitch

$$h\boldsymbol{\omega} = \mathbf{v} \quad \Rightarrow \quad h = \frac{\boldsymbol{\omega}^T \mathbf{v}}{\boldsymbol{\omega}^T \boldsymbol{\omega}}. \quad (3)$$

A wrench is the force and moment acting on a body at a point. It is a six-vector $\mathbf{w} = [\mathbf{f}^T \boldsymbol{\tau}^T]^T$ where $\mathbf{f}^T = [f_x \ f_y \ f_z]$ is force and $\boldsymbol{\tau}^T = [\tau_x \ \tau_y \ \tau_z]$ is torque. The screw representation of a wrench is

$$\begin{aligned} \mathbf{q} &= \frac{\mathbf{f} \times \boldsymbol{\tau}}{\mathbf{f}^T \mathbf{f}} \quad \mathbf{w} = \mathbf{f} \text{ if } \mathbf{f} \neq \mathbf{0} \\ \mathbf{q} &= \mathbf{0} \quad \mathbf{w} = \boldsymbol{\tau} \text{ if } \mathbf{f} = \mathbf{0} \end{aligned} \quad (4)$$

magnitude

$$\begin{aligned} M &= \|\mathbf{f}\| \text{ if } \mathbf{f} \neq \mathbf{0} \\ M &= \|\boldsymbol{\tau}\| \text{ if } \mathbf{f} = \mathbf{0} \end{aligned} \quad (5)$$

pitch

$$h\mathbf{f} = \boldsymbol{\tau} \quad \Rightarrow \quad h = \frac{\mathbf{f}^T \boldsymbol{\tau}}{\mathbf{f}^T \mathbf{f}}. \quad (6)$$

B. Spatial Stiffness Matrix

Hooke famously modelled a simple unstretched linear spring. The work done $U(x)$ in stretching or compressing the spring by a small amount x is given by $U(x) = (1/2)kx^2$ where k is a scalar constant. Taking the gradient of the potential yields the force acting on the spring $F = \nabla U(x) = kx$ which is Hooke's law. Note that the Hessian of $U(x)$ is k .

Calculating the force exerted on a body by taking the gradient of a potential scalar field is a general principle in physics. For example, the force of gravity on a body with mass, and the force an electric field exerts on a charged particle, are two instances where forces can be associated with potential energy. More generally, both the net force and torque exerted on a body are required. The stiffness matrix \mathbf{K} relates wrenches (force and torque) to small twist displacements as

$$\begin{aligned} \mathbf{w} &= \mathbf{K} \mathbf{t} \\ \text{force } \begin{bmatrix} \mathbf{f} \\ \boldsymbol{\tau} \end{bmatrix} &= \begin{bmatrix} \mathbf{A} & \mathbf{B} \\ \mathbf{B}^T & \mathbf{D} \end{bmatrix} \begin{bmatrix} \mathbf{v} \\ \boldsymbol{\omega} \end{bmatrix} \begin{matrix} \text{linear displ.} \\ \text{rotational displ.} \end{matrix} \end{aligned} \quad (7)$$

which is a generalization of Hooke's law. Observe that force is dependent on rotational displacement via the submatrix \mathbf{B} , and torque is dependent on linear displacement via the submatrix \mathbf{B}^T . If \mathbf{B} is nonzero then the rotational and translational aspects of stiffness are coupled.

The inverse relationship of stiffness is compliance, which relates twists to wrenches. The compliance matrix, \mathbf{C} , is the inverse of the stiffness matrix, \mathbf{K}^{-1}

$$\begin{aligned} \mathbf{t} &= \mathbf{C} \mathbf{w} \\ \begin{bmatrix} \mathbf{v} \\ \boldsymbol{\omega} \end{bmatrix} &= \begin{bmatrix} \mathbf{E} & \mathbf{G} \\ \mathbf{G}^T & \mathbf{H} \end{bmatrix} \begin{bmatrix} \mathbf{f} \\ \boldsymbol{\tau} \end{bmatrix}. \end{aligned} \quad (8)$$

The spatial-stiffness and compliance matrices are often used to analyze the elastic behavior of a mechanism about an equilibrium state. Consider an unloaded, unactuated, kinematically unconstrained rigid body elastically suspended in space by a parallel network of simple springs. In this situation the stiffness matrix will be symmetric because two opposite twists of equal magnitude should cancel around the equilibrium configuration, and \mathbf{K} is given by the Hessian of the potential energy $U(\mathbf{t})$. \mathbf{K} is positive definite¹ because an agent must do positive work (expend energy) to produce a displacement of the mechanism.

1) *Structure of the Stiffness Matrix:* Several approaches to studying the structure of the spatial-stiffness matrix have previously been summarized [28].

The recent analysis of the structure of the spatial-stiffness matrix originated with Loncarić [29] who used a Lie group approach to derive a normal form of the stiffness matrix. Loncarić chose to define the normal form as the one that maximally decoupled the rotational and translational components of stiffness; that is, a stiffness matrix in normal form has the simplest form of \mathbf{B} . He showed that, in normal form, \mathbf{A} and \mathbf{D} are symmetric and \mathbf{B} is diagonal. This was accomplished by deriving the formula for transforming a stiffness matrix by a rigid change of coordinate frame, and considering the effect of such a transformation on \mathbf{B} . The origin of the transformed frame was called the center of stiffness. The normal form is not unique [28]: it is possible to diagonalize either \mathbf{A} or \mathbf{D} and have symmetric \mathbf{B} . It has been shown that any symmetric positive semi-definite stiffness matrix can be written in normal form [30].

Patterson and Lipkin [31] examined the structure of compliance matrices by looking for twists and wrenches that were multiples of the same screw, that is to say, they analyzed the eigenvalue problem for compliance matrices. They established several properties of the eigenvalues and eigenscrews but admitted that "practice there are few direct applications for eigenscrews" (p. 578). They went on to describe a more practical analysis based on the concept of a compliant axis.

The definition of compliant axis was given as: "A compliant axis exists when a force produces a parallel linear deformation, and rotational deformation about the line of the force produces a parallel couple" [32, p. 582]. This contrasts sharply with the general case where a force produces a nonparallel translation and a rotational displacement. The compliant axis was generalized to the partial compliant axis, twist compliant axis, and wrench compliant axis in subsequent work [31].

Twist-compliant and wrench-compliant axes are fundamental to the approach used in this article to analyze fiducial registra-

¹If it is possible for an agent to do zero work to displace the mechanism then \mathbf{K} is positive semi-definite.

tion. A twist-compliant axis is one where a twist deformation about the axis produces a pure torque parallel to the axis. This can be expressed as an eigenvalue problem

$$\mu_i \begin{bmatrix} \mathbf{0} \\ \boldsymbol{\omega} \end{bmatrix} = \mathbf{K} \begin{bmatrix} \mathbf{v} \\ \boldsymbol{\omega} \end{bmatrix} \quad (9)$$

which can be solved by premultiplying both sides by $(1/\mu_i)\mathbf{K}^{-1} = (1/\mu_i)\mathbf{C}$

$$\mathbf{C} \begin{bmatrix} \mathbf{0} \\ \boldsymbol{\omega} \end{bmatrix} = \frac{1}{\mu_i} \begin{bmatrix} \mathbf{v} \\ \boldsymbol{\omega} \end{bmatrix}. \quad (10)$$

Substituting (8) leads to an eigenvalue problem involving the 3×3 matrix \mathbf{H}

$$\mathbf{H}\boldsymbol{\omega} = \frac{1}{\mu_i}\boldsymbol{\omega} \quad (11)$$

where the three eigenvalues $1/\mu_i$ of \mathbf{H} are the rotational compliances (and the μ_i are the rotational stiffnesses). The three twists $[\mathbf{v}_i^T \ \boldsymbol{\omega}_i^T]^T$ obtained by substituting the eigenvalues and eigenvectors into (10) are called eigentwists. An eigentwist produces a pure torque about the twist-compliant axis.

A wrench-compliant axis is one for which a force parallel to the axis produces a pure linear displacement that is parallel to the axis. It is associated with the eigenvalue problem

$$\frac{1}{\sigma_i} \begin{bmatrix} \mathbf{f} \\ \mathbf{0} \end{bmatrix} = \mathbf{C} \begin{bmatrix} \mathbf{f} \\ \boldsymbol{\tau} \end{bmatrix} \quad (12)$$

which can be solved by premultiplying both sides by $\sigma_i\mathbf{C}^{-1} = \sigma_i\mathbf{K}$

$$\mathbf{K} \begin{bmatrix} \mathbf{f} \\ \mathbf{0} \end{bmatrix} = \sigma_i \begin{bmatrix} \mathbf{f} \\ \boldsymbol{\tau} \end{bmatrix}. \quad (13)$$

Substituting (7) into (13) leads to an eigenvalue problem involving the 3×3 matrix \mathbf{A}

$$\mathbf{A}\mathbf{f} = \sigma_i\mathbf{f} \quad (14)$$

where the three eigenvalues σ_i of \mathbf{A} are the linear stiffnesses (and the $1/\sigma_i$ are the linear compliances). The three wrenches $[\mathbf{f}_i^T \ \boldsymbol{\tau}_i^T]^T$ obtained by substituting the eigenvalues and eigenvectors (13) are called eigenwrenches. An eigenwrench produces a pure linear translation in the direction of a wrench-compliant axis.

A configuration-space approach was used by Lin *et al.* [27] to quantify the quality of a compliant grasp or fixture; in doing so, the authors managed to rederive the rotational and linear stiffnesses, and the twist and wrench-compliant axes [31]. To derive the rotational stiffnesses and the twist-compliant axes, they looked for the subspace V of small displacements that produced pure torque (or zero force)

$$\mathbf{f} = \mathbf{0} = \mathbf{A}\mathbf{v} + \mathbf{B}\boldsymbol{\omega} \Rightarrow \mathbf{v} = -\mathbf{A}^{-1}\mathbf{B}\boldsymbol{\omega}. \quad (15)$$

This implies that V is the set of twists parameterized by rotational displacement

$$V = \{\mathbf{t} = \mathbf{P}\boldsymbol{\omega}\}, \quad \text{where } \mathbf{P} = \begin{bmatrix} -\mathbf{A}^{-1}\mathbf{B} \\ \mathbf{I} \end{bmatrix}. \quad (16)$$

It was shown that the restriction of the stiffness matrix to the subspace V is given by

$$\mathbf{K}_V = \mathbf{P}^T\mathbf{K}\mathbf{P} = \mathbf{D} - \mathbf{B}^T\mathbf{A}^{-1}\mathbf{B}. \quad (17)$$

The inverse of a matrix \mathbf{X} partitioned into blocks is given by [33] as

$$\mathbf{X} = \begin{bmatrix} \mathbf{X}_{11} & \mathbf{X}_{12} \\ \mathbf{X}_{21} & \mathbf{X}_{22} \end{bmatrix} \quad \mathbf{X}^{-1} = \begin{bmatrix} \mathbf{X}'_{11} & \mathbf{X}'_{12} \\ \mathbf{X}'_{21} & \mathbf{X}'_{22} \end{bmatrix}$$

where

$$\begin{aligned} \mathbf{X}'_{11} &= [\mathbf{X}_{11} - \mathbf{X}_{12}\mathbf{X}_{22}^{-1}\mathbf{X}_{21}]^{-1} \\ \mathbf{X}'_{12} &= \mathbf{X}_{11}^{-1}\mathbf{X}_{12}[\mathbf{X}_{21}\mathbf{X}_{11}^{-1}\mathbf{X}_{12} - \mathbf{X}_{22}]^{-1} \\ \mathbf{X}'_{21} &= [\mathbf{X}_{21}\mathbf{X}_{11}^{-1}\mathbf{X}_{12} - \mathbf{X}_{22}]^{-1}\mathbf{X}_{21}\mathbf{X}_{11}^{-1} \\ \mathbf{X}'_{22} &= [\mathbf{X}_{22} - \mathbf{X}_{21}\mathbf{X}_{11}^{-1}\mathbf{X}_{12}]^{-1}. \end{aligned} \quad (18)$$

Inspection of the lower-right block of (18) leads to the conclusion that

$$\mathbf{K}_V = \mathbf{D} - \mathbf{B}^T\mathbf{A}^{-1}\mathbf{B} = \mathbf{H}^{-1}. \quad (19)$$

Recall that (11) defines the directions of a twist-compliant axes as the eigenvectors $\boldsymbol{\omega}_i$ of \mathbf{H} and the rotational compliances as the eigenvalues $1/\mu_i$ of \mathbf{H} . Because $\mathbf{K}_V = \mathbf{H}^{-1}$, the eigenvectors of \mathbf{K}_V are the same as the eigenvectors of \mathbf{H} , and the eigenvalues of \mathbf{K}_V are the reciprocals of the eigenvalues of \mathbf{H} ; thus, the eigenvalues of \mathbf{K}_V are the rotational stiffnesses μ_i . The μ_i were named the principal rotational stiffnesses, and they proved that the stiffnesses were invariant under a rigid coordinate frame transformation by applying the coordinate frame transformation law of stiffness matrices to \mathbf{K}_V .

To derive the translational stiffnesses and the wrench-compliant axes, Lin *et al.* [27] looked for the subspace W of wrenches that produced pure translation (or zero rotational displacement)

$$\boldsymbol{\omega} = \mathbf{0} = \mathbf{G}^T\mathbf{f} + \mathbf{H}\boldsymbol{\tau} \Rightarrow \boldsymbol{\tau} = -\mathbf{H}^{-1}\mathbf{G}^T\mathbf{f}. \quad (20)$$

This implies that W is the set of wrenches parameterized by force

$$W = \{\mathbf{w} = \mathbf{Q}\mathbf{f}\} \quad \text{where } \mathbf{Q} = \begin{bmatrix} \mathbf{I} \\ -\mathbf{H}^{-1}\mathbf{G}^T \end{bmatrix}. \quad (21)$$

It was shown that the restriction of the compliance matrix to the subspace W is given by

$$\mathbf{C}_W = \mathbf{Q}^T\mathbf{C}\mathbf{Q} = \mathbf{E} - \mathbf{G}\mathbf{H}^{-1}\mathbf{G}^T. \quad (22)$$

Inspection of the upper-left block of (18) leads to the conclusion that

$$\mathbf{C}_W = \mathbf{E} - \mathbf{G}\mathbf{H}^{-1}\mathbf{G}^T = \mathbf{A}^{-1}. \quad (23)$$

Recall that (14) defines the directions of a wrench-compliant axes as the eigenvectors \mathbf{f}_i of \mathbf{A} and the linear stiffnesses as the eigenvalues σ_i of \mathbf{A} . Because $\mathbf{C}_W = \mathbf{A}^{-1}$, the eigenvectors

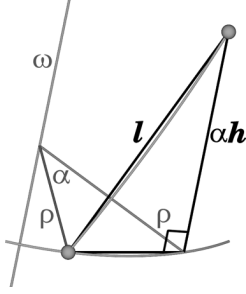


Fig. 1. The displacement of a point under a screw motion. The point rotates by an amount α about the axis with direction ω , then translates parallel to the axis by an amount αh . The net distance of displacement is l .

of \mathbf{C}_W are the same as the eigenvectors of \mathbf{A} , and the eigenvalues of \mathbf{C}_W are the reciprocals of the eigenvalues of \mathbf{A} ; thus, the eigenvalues of \mathbf{C}_W are the linear compliances $1/\sigma_i$. The σ_i were named the principal translational stiffnesses, and they proved that the stiffnesses were invariant under a rigid coordinate frame transformation.

A frame invariant quality measure of compliant grasps based on the smallest principal stiffness was also derived [27]. To do so, a meaningful way to compare the translational and rotational stiffnesses was formulated by considering the deflection of the grasped object. Consider a twist displacement of magnitude α about the screw axis $[\mathbf{v}_i^T \ \boldsymbol{\omega}_i^T]^T$ where $\boldsymbol{\omega}_i$ is an eigenvector of \mathbf{K}_V and \mathbf{v}_i is given by (15). A point located distance ρ from the screw axis will be displaced by length

$$\begin{aligned} l &= \sqrt{\rho^2 + \rho^2 - 2\rho^2 \cos \alpha + (\alpha h)^2} \quad (\text{law of cosines}) \\ &\approx \sqrt{2\rho^2 - 2\rho^2 \left(1 - \frac{\alpha^2}{2}\right) + \alpha^2(\boldsymbol{\omega} \cdot \mathbf{v})^2} \\ &= |\alpha| \sqrt{\rho^2 + (\boldsymbol{\omega} \cdot \mathbf{v})^2} \end{aligned} \quad (24)$$

where the approximation is the Maclaurin series approximation. This is illustrated in Fig. 1. Because the twist is about a twist-compliant axis, it generates pure torque and the potential energy associated with the displacement is $(1/2)\mu_i\alpha^2$ (the potential energy associated with a torsional spring with spring constant μ_i displaced by α radians). The rotational stiffness is converted to its equivalent linear stiffness by associating the displacement magnitude l with a linear spring of stiffness $\mu_{\text{eq},i}$; the potential energy is $(1/2)\mu_{\text{eq},i}l^2$ and it must be equal to $(1/2)\mu_i\alpha^2$. This yields the equivalent rotational stiffnesses

$$\mu_{\text{eq},i} = \frac{\mu_i}{(\rho_i^2 + (\boldsymbol{\omega}_i \cdot \mathbf{v}_i)^2)} \quad i = 1, 2, 3 \quad (25)$$

which can be compared directly to the principal linear stiffnesses. The stiffness quality measure is defined as

$$Q = \min(\mu_{\text{eq},1}, \mu_{\text{eq},2}, \mu_{\text{eq},3}, \sigma_1, \sigma_2, \sigma_3) \quad (26)$$

Q characterizes the least constrained displacement of the mechanism; maximizing Q will minimize the worst-case displacement of the mechanism.

III. METHOD

A. Spatial Stiffness Matrix for Fiducial Registration

A spatial-stiffness model of fiducial registration treats the markers as a passive rigid mechanism suspended by linear springs. The springs elongate and compress to exert a restoring force if the markers are displaced. The amount of extension of the springs, and hence the energy stored in the springs, is determined by the FLE.

We also assume that the N noise-free fiducial marker locations $\{\mathbf{p}_1, \mathbf{p}_2, \dots, \mathbf{p}_N\}$, where $\mathbf{p}_j = [x_j \ y_j \ z_j]^T$, are known. We also assume that the 3D FLE for the j th fiducial can be modeled as a zero-mean Gaussian variable with covariance matrix $\boldsymbol{\Sigma}_j$. The covariance matrices are expressed in the same coordinate frame as the marker locations.

Consider the situation where $\boldsymbol{\Sigma}_j$ is the diagonal matrix $\text{diag}(s_{x_j}^2, s_{y_j}^2, s_{z_j}^2)$ (the fiducial localization noise is aligned with the x -, y -, and z -axes) with variances $s_{x_j}^2$, $s_{y_j}^2$, and $s_{z_j}^2$. Our model uses linear springs aligned in the x -, y -, and z -directions to represent the effect of FLE. The spring constants k_{x_j} , k_{y_j} , and k_{z_j} are chosen to be equal to the reciprocals of the variances in order to model anisotropy in the noise. A linear spring resists displacements only in directions parallel to its length; thus, the force-displacement relationships of the three springs can be written as

$$\begin{aligned} \mathbf{f}_x &= \begin{bmatrix} k_{x_j} & 0 & 0 \\ 0 & 0 & 0 \\ 0 & 0 & 0 \end{bmatrix} \mathbf{v}, \mathbf{f}_y = \begin{bmatrix} 0 & 0 & 0 \\ 0 & k_{y_j} & 0 \\ 0 & 0 & 0 \end{bmatrix} \mathbf{v}, \\ \mathbf{f}_z &= \begin{bmatrix} 0 & 0 & 0 \\ 0 & 0 & 0 \\ 0 & 0 & k_{z_j} \end{bmatrix} \mathbf{v} \end{aligned}$$

for a small linear displacement \mathbf{v} . The net force of the system of springs is just the sum of the three forces, or

$$\mathbf{f} = \begin{bmatrix} k_{x_j} & 0 & 0 \\ 0 & k_{y_j} & 0 \\ 0 & 0 & k_{z_j} \end{bmatrix} \mathbf{v} = \begin{bmatrix} \frac{1}{s_{x_j}^2} & 0 & 0 \\ 0 & \frac{1}{s_{y_j}^2} & 0 \\ 0 & 0 & \frac{1}{s_{z_j}^2} \end{bmatrix} \mathbf{v}. \quad (27)$$

Note that the 3×3 diagonal matrix in the preceding equation is the submatrix \mathbf{A} of \mathbf{K} in (7) that relates linear displacements to force; thus, we have

$$\mathbf{f} = \tilde{\mathbf{A}}_j \mathbf{v}, \quad (28)$$

where $\tilde{\mathbf{A}}_j$ is the matrix of spring constants for axis aligned noise.

For an arbitrary $\boldsymbol{\Sigma}_j$, we align the springs in the directions of the principal components of $\boldsymbol{\Sigma}_j$ and assign spring constants equal to the reciprocals of the variances of the principal components. To do so, we use the fact that $\boldsymbol{\Sigma}_j$ can be diagonalized by a change of coordinates represented by a rotation matrix \mathbf{Q}_j [34]

$$\mathbf{Q}_j^T \boldsymbol{\Sigma}_j \mathbf{Q}_j = \begin{bmatrix} s_{x_j}^2 & 0 & 0 \\ 0 & s_{y_j}^2 & 0 \\ 0 & 0 & s_{z_j}^2 \end{bmatrix}, \quad (29)$$

where \mathbf{Q}_j is the matrix of normalized eigenvectors of Σ_j and the eigenvalues $s_{x_j}^2$, $s_{y_j}^2$, and $s_{z_j}^2$ of Σ_j are the variances of the principal components. We use three facts about matrices [33].

- Because Σ_j is a positive definite Hermitian matrix, Σ_j^{-1} is also a positive definite Hermitian matrix; hence, it is also a covariance matrix.
 - The eigenvectors of a matrix and its inverse are the same.
 - The eigenvalues of a matrix and its inverse are reciprocals.
- These three facts imply that \mathbf{Q}_j diagonalizes Σ_j^{-1} such that

$$\mathbf{Q}_j^T \Sigma_j^{-1} \mathbf{Q}_j = \begin{bmatrix} \frac{1}{s_{x_j}^2} & 0 & 0 \\ 0 & \frac{1}{s_{y_j}^2} & 0 \\ 0 & 0 & \frac{1}{s_{z_j}^2} \end{bmatrix} = \tilde{\mathbf{A}}_j, \quad (30)$$

which is the matrix of spring constants for axis aligned noise from (27). To align $\tilde{\mathbf{A}}_j$ with the actual noise, we need to perform a change of coordinates represented by \mathbf{Q}_j^{-1} , the inverse of the diagonalizing rotation. A rigid change of coordinates affects the submatrix \mathbf{A} of a stiffness matrix \mathbf{K} according to $\mathbf{Q}^T \mathbf{A} \mathbf{Q}$ where \mathbf{Q} is the rotation part of the rigid transformation [28]; therefore, the desired matrix of spring constants is

$$\mathbf{A}_j = (\mathbf{Q}_j^{-1})^T \tilde{\mathbf{A}}_j \mathbf{Q}_j^{-1} = (\mathbf{Q}_j^{-1})^T \mathbf{Q}_j^T \Sigma_j^{-1} \mathbf{Q}_j \mathbf{Q}_j^{-1} = \Sigma_j^{-1}. \quad (31)$$

The spatial stiffness matrix is derived by applying an infinitesimal rigid displacement to the mechanism and computing the Hessian of the potential energy stored in the linear springs. Let the rigid displacement be made up of a small rotation $\mathbf{R} = \mathbf{R}_z(\omega_z) \mathbf{R}_y(\omega_y) \mathbf{R}_x(\omega_x)$ followed by a small translation $\boldsymbol{\delta} = [\delta_x \ \delta_y \ \delta_z]^T$. The locations \mathbf{m}_j of the displaced markers are given by $\mathbf{m}_j = \mathbf{R} \mathbf{p}_j + \boldsymbol{\delta}$. The potential energy stored in the springs associated with the marker is

$$\begin{aligned} U_j &= \frac{1}{2} (\mathbf{m}_j - \mathbf{p}_j)^T \mathbf{A}_j (\mathbf{m}_j - \mathbf{p}_j) \\ &= \frac{1}{2} (\mathbf{m}_j - \mathbf{p}_j)^T \Sigma_j^{-1} (\mathbf{m}_j - \mathbf{p}_j) \end{aligned} \quad (32)$$

which is proportional to the squared Mahalanobis distance between \mathbf{p}_j and \mathbf{m}_j . It can be shown that the Hessian \mathbf{H}_j of U_j evaluated at zero displacement is

$$\begin{aligned} \mathbf{H}_j &= \mathbf{H}(U_j; \omega_x = \omega_y = \omega_z = t_x = t_y = t_z = 0) \\ &= \begin{bmatrix} \mathbf{A}_j & \mathbf{B}_j \\ \mathbf{B}_j^T & \mathbf{D}_j \end{bmatrix} \quad \text{where} \quad \mathbf{A}_j = \Sigma_j^{-1} \end{aligned} \quad (33)$$

$$\mathbf{B}_j = \Sigma_j^{-1} \begin{bmatrix} 0 & -z_j & y_j \\ z_j & 0 & -x_j \\ -y_j & x_j & 0 \end{bmatrix}^T \quad (34)$$

$$\mathbf{D}_j = \begin{bmatrix} 0 & -z_j & y_j \\ z_j & 0 & -x_j \\ -y_j & x_j & 0 \end{bmatrix} \Sigma_j^{-1} \begin{bmatrix} 0 & -z_j & y_j \\ z_j & 0 & -x_j \\ -y_j & x_j & 0 \end{bmatrix}^T. \quad (35)$$

The stiffness matrix is $\mathbf{K} = \sum_{j=1}^N \mathbf{H}_j$.

B. TRE Estimation

We hypothesize that TRE can be estimated by considering a constant amount of work done, c , and calculating the displacement of the system. The work done is taken to be the sum $c = c_\delta + c_r$ of two constant components $c_\delta = c_r$ representing the energies required to respectively translate and rotate the system. Our hypothesis is based on the work of Lin *et al.* [27] who showed that the stiffnesses define the geometry of the level-sets related to the elastic energy induced by compliant deformations.

Suppose that the elastic system of fiducial markers is translated by an amount α_{δ_1} in a direction parallel to \mathbf{v}_1 where \mathbf{v}_1 is the eigenvector associated with the principal translational stiffness σ_1 . Such a translation will induce a TRE of magnitude α_{δ_1} . The work done by this translation is $(1/2)\sigma_1\alpha_{\delta_1}^2$; simple rearrangement yields the squared displacement per unit work done $\alpha_{\delta_1}^2 = 2/\sigma_1$. A similar argument can be used to obtain $\alpha_{\delta_2}^2 = 2/\sigma_2$ and $\alpha_{\delta_3}^2 = 2/\sigma_3$, the squared displacements per unit work done in the directions parallel to \mathbf{v}_2 and \mathbf{v}_3 , respectively. The squared translational TRE (per unit work done) is

$$\alpha_\delta^2 = \alpha_{\delta_1}^2 + \alpha_{\delta_2}^2 + \alpha_{\delta_3}^2 = 2 \left(\frac{1}{\sigma_1} + \frac{1}{\sigma_2} + \frac{1}{\sigma_3} \right). \quad (36)$$

Suppose the system is rotated about the axis $\boldsymbol{\omega}_1$ where $\boldsymbol{\omega}_1$ is the eigenvector associated with the principal rotational stiffness μ_1 . Such a rotation will induce a TRE of magnitude α_{r_1} . The work done by this rotation is $(1/2)\mu_{\text{eq}_1}\alpha_{r_1}^2$; simple rearrangement yields the squared displacement per unit work done $\alpha_{r_1}^2 = 2/\mu_{\text{eq}_1}$. Using a similar argument for rotations about $\boldsymbol{\omega}_2$ and $\boldsymbol{\omega}_3$ leads to a total squared displacement per unit work done of

$$\alpha_r^2 = \alpha_{r_1}^2 + \alpha_{r_2}^2 + \alpha_{r_3}^2 = 2 \left(\frac{1}{\mu_{\text{eq}_1}} + \frac{1}{\mu_{\text{eq}_2}} + \frac{1}{\mu_{\text{eq}_3}} \right). \quad (37)$$

Assuming independence of the rotational and translational components allows us to write the expected squared TRE per unit energy for a target location \mathbf{r} as

$$\begin{aligned} \text{TRE}^2(\mathbf{r}) &= \alpha_t^2 + \alpha_r^2 \\ &= \frac{1}{\sigma_1} + \frac{1}{\sigma_2} + \frac{1}{\sigma_3} + \frac{1}{\mu_{\text{eq}_1}} + \frac{1}{\mu_{\text{eq}_2}} + \frac{1}{\mu_{\text{eq}_3}}. \end{aligned} \quad (38)$$

1) *Identical Isotropic FLE*: Equation (38) can be simplified significantly if the fiducial localization noise distribution is identical and isotropic. Because the principal stiffnesses are frame invariant, we can apply any rigid change of coordinate frame without affecting the estimated TRE. Let us choose a coordinate frame such that the origin is the mean of the fiducial locations; that is, $\sum_{j=1}^N x_j = \sum_{j=1}^N y_j = \sum_{j=1}^N z_j = 0$. Let the total FLE magnitude be s_{FLE} ; then the noise covariance for the j th fiducial is the diagonal matrix $\Sigma_j = (s_{\text{FLE}}^2/3)\mathbf{I}_{3 \times 3}$ where $\mathbf{I}_{3 \times 3}$ is the 3×3 identity matrix. Using (33)–(35) gives a stiffness matrix

$$\mathbf{K} = \begin{bmatrix} \mathbf{A} & \mathbf{B} \\ \mathbf{B}^T & \mathbf{D} \end{bmatrix} \quad \text{where} \quad \mathbf{A} = \frac{3N}{s_{\text{FLE}}^2} \mathbf{I}_{3 \times 3} \quad (39)$$

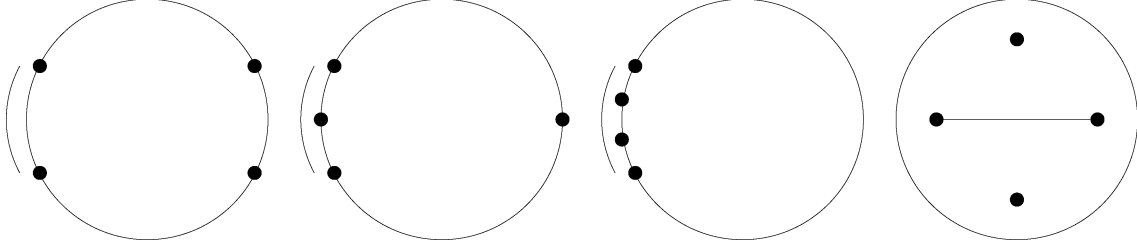


Fig. 2. Fiducial configurations on a sphere of radius 100 mm centered at the origin. In cases *A*, *B*, and *C*, the fiducials are located in the xy -plane and d is the indicated arc length. In case *D*, the fiducials are located in a plane parallel to the xy -plane and d is the diagonal distance of the square arrangement of markers.

$$\mathbf{B} = \frac{3}{s_{\text{FLE}}^2} \sum_{j=1}^N \begin{bmatrix} 0 & z_j & -y_j \\ -z_j & 0 & x_j \\ y_j & -x_j & 0 \end{bmatrix} = [\mathbf{0}] \quad (40)$$

$$\mathbf{D} = \frac{3}{s_{\text{FLE}}^2} \sum_{j=1}^N \begin{bmatrix} y_j^2 + z_j^2 & -x_j y_j & -x_j z_j \\ -x_j y_j & x_j^2 + z_j^2 & -y_j z_j \\ -x_j z_j & -y_j z_j & x_j^2 + y_j^2 \end{bmatrix}. \quad (41)$$

The principal translational stiffnesses are the eigenvalues of (39); thus, $\sigma_{i=1,2,3} = 3N/s_{\text{FLE}}^2$. The principal rotational stiffnesses are the eigenvalues of $\mathbf{K}_V = \mathbf{D} - \mathbf{B}^T \mathbf{A}^{-1} \mathbf{B} = \mathbf{D}$. Observe that \mathbf{D} is the inertia tensor of a system of N point particles of unit mass [35]; thus, the rotational stiffnesses are the principal moments of inertia and the eigenvectors are the principal axes. The equivalent rotational stiffnesses are given by (25). Because $\mathbf{B} = [\mathbf{0}]$, (15) implies that $\mathbf{v}_i = \mathbf{0}$; thus, the equivalent rotational stiffnesses are $\mu_{\text{eq},i=1,2,3} = 3\mu_i/(s_{\text{FLE}}^2 \rho_i^2)$ where μ_i is the i th principal moment of inertia and ρ_i^2 is the squared distance between the target and the i th principal axis of inertia. Equation (38) becomes

$$\text{TRE}^2(\mathbf{r}) = s_{\text{FLE}}^2 \left(\frac{1}{N} + \frac{1}{3} \sum_{i=1}^3 \frac{\rho_i^2}{\mu_i} \right). \quad (42)$$

Fitzpatrick *et al.* gave their expression (46) in [2] as

$$\langle \text{TRE}^2(\mathbf{r}) \rangle \approx \frac{\langle \text{FLE}^2 \rangle}{N} \left(1 + \frac{1}{3} \sum_{k=1}^3 \frac{d_k^2}{f_k^2} \right) \quad (43)$$

where $\langle \text{FLE}^2 \rangle$ is the expected value of the squared fiducial localization error, d_k is the distance between the target and the k th principal axis, f_k is the rms distance of the fiducials from the k th principal axis, and $N f_k^2$ is the moment of inertia about the k th principal axis. Equation (42) and (43) are equivalent if the fiducial localization noise is zero mean ($\langle \text{FLE} \rangle = 0$) because by definition $s_{\text{FLE}}^2 = \langle (\text{FLE} - \langle \text{FLE} \rangle)^2 \rangle$.

C. Summary

The parameters of our model are as follows.

- The N noise-free fiducial marker locations $\{\mathbf{p}_1, \mathbf{p}_2, \dots, \mathbf{p}_N\}$, where $\mathbf{p}_j = [x_j \ y_j \ z_j]^T$.
- The covariances of FLE Σ_j at each marker location.
- The target location \mathbf{r} where the TRE magnitude is desired.

The method for computing (38) is summarized in the following list.

- 1) Compute the stiffness matrix $\mathbf{K} = \begin{bmatrix} \mathbf{A} & \mathbf{B} \\ \mathbf{B}^T & \mathbf{D} \end{bmatrix}$ using (33)–(35).

- 2) Compute the eigenvalues and eigenvectors of $\mathbf{D} - \mathbf{B}^T \mathbf{A}^{-1} \mathbf{B}$; see (17). The eigenvalues are the principal rotational stiffnesses μ_1 , μ_2 , and μ_3 . The eigenvectors $\boldsymbol{\omega}_1$, $\boldsymbol{\omega}_2$, and $\boldsymbol{\omega}_3$ are the rotational components of the eigentwists.
- 3) Compute the translational components \mathbf{v}_1 , \mathbf{v}_2 , and \mathbf{v}_3 of the eigentwists using (15).
- 4) Compute the axis of the screw representation of each eigentwist $[\mathbf{v}_i^T \ \boldsymbol{\omega}_i^T]^T$ for $i = 1, 2, 3$ using (1).
- 5) Compute the squared distances ρ_1^2 , ρ_2^2 , ρ_3^2 between the screw axis and the target location \mathbf{r} .
- 6) Compute the eigenvalues of \mathbf{A} ; see (23). The eigenvalues are the principal translational stiffnesses σ_1 , σ_2 , and σ_3 .
- 7) Compute $\text{TRE}^2(\mathbf{r})$ using (38).

IV. EXPERIMENTAL VALIDATION

A. Heteroscedastic Fiducial Localization Noise

We validated (38) by performing simulations similar to the ones described by Maurer *et al.* [36]. We used four configurations of fiducial markers, shown in Fig. 2, arranged on a sphere of radius 100 mm. The input to each simulation was the set of marker locations $\{\mathbf{p}_{j=1,2,3,4}\}$ parameterized by a scalar length d (see Fig. 2), a target location \mathbf{r} , and the covariances Σ_j of the fiducial localization noise. The output was the squared TRE for each target. Each simulation was run for 10 000 trials, with the k th trial executing the following steps:

- 1) Noisy marker locations $\mathbf{m}_{j,k}$ were generated by adding Gaussian distributed noise $\mathcal{N}(0, \Sigma_j)$ to \mathbf{p}_j .
- 2) $\{\mathbf{m}_{j,k}\}$ was registered to $\{\mathbf{p}_j\}$ using the HEIV and Horn's methods to obtain the registration rotation \mathbf{R}_k and translation \mathbf{d}_k .
- 3) Squared TRE was computed as the dot product $\boldsymbol{\delta}_k \cdot \boldsymbol{\delta}_k$ where $\boldsymbol{\delta}_k = \mathbf{r} - (\mathbf{R}_k \mathbf{r} + \mathbf{d}_k)$.

The rms TRE was computed as $\text{TRE}_{\text{rms}} = \sqrt{(1/10000) \sum_{k=1}^{10000} (\boldsymbol{\delta}_k \cdot \boldsymbol{\delta}_k)}$.

Consider the location of \mathbf{p}_j given in spherical coordinates (r, θ_j, ϕ) where $r = 100$ mm is the radial distance, θ_j is the azimuth angle measured from the x -axis, and ϕ is the polar angle measured from the positive z -axis. For configurations *A*–*C*, $\phi = \pi$ radians for each marker (the markers all lie on a great circle of a sphere with radius of 100 mm); for configuration *D*, ϕ is a function of d and identical for each marker. We defined four FLE covariance matrices (one for each of the markers \mathbf{p}_j)

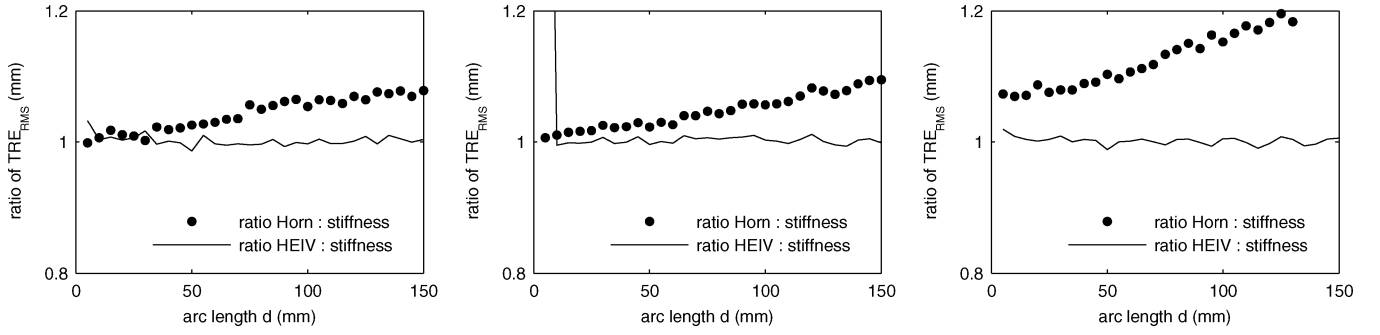


Fig. 3. The ratios of simulated to predicted TRE_{rms} values for fiducial configurations A , B , and D with target location $\mathbf{r} = [50 \ 50 \ 50]^T$.

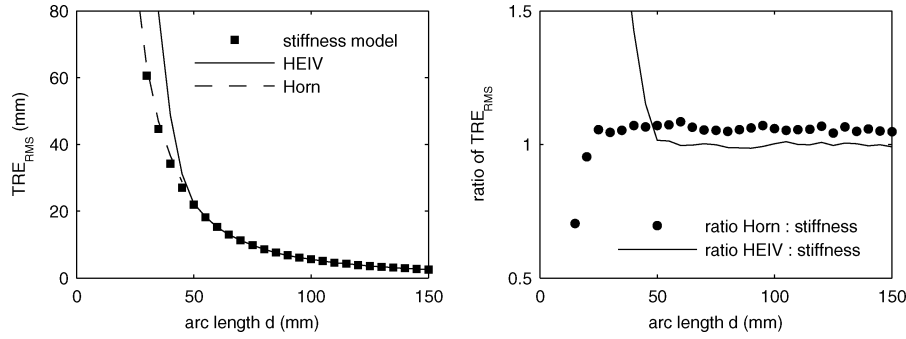


Fig. 4. (Left) Simulated and predicted TRE_{rms} values for fiducial configuration C with target location $\mathbf{r} = [50 \ 50 \ 50]^T$. (Right) Ratios of simulated to predicted TRE_{rms} values for configuration C .

$$\begin{aligned} \Sigma'_1 &= \begin{bmatrix} a^2 & & \\ & a^2 & \\ & & a^2 \end{bmatrix} & \Sigma'_2 &= \begin{bmatrix} a^2 & & \\ & b^2 & \\ & & c^2 \end{bmatrix} \\ \Sigma'_3 &= \begin{bmatrix} b^2 & & \\ & a^2 & \\ & & c^2 \end{bmatrix} & \Sigma'_4 &= \begin{bmatrix} c^2 & & \\ & b^2 & \\ & & a^2 \end{bmatrix} \end{aligned} \quad (44)$$

where the values $a^2 = (0.35 \text{ mm})^2$, $b^2 = (0.1 \text{ mm})^2$, and $c^2 = (0.5 \text{ mm})^2$ were chosen arbitrarily; the fiducial localization noise covariances Σ_j were rotated versions of Σ'_j . For configurations A – C , the noise covariances were defined as

$$\Sigma_j = \mathbf{R}_z(\theta_j) \Sigma'_j \mathbf{R}_z^T(\theta_j) \quad (45)$$

where $\mathbf{R}_z(\theta_j)$ was the rotation about the z -axis by angle θ_j . For configuration D , the noise covariances were defined as

$$\begin{aligned} \Sigma_1 &= \mathbf{R}_x(-\phi) \Sigma'_1 \mathbf{R}_x^T(-\phi) \\ \Sigma_2 &= \mathbf{R}_y(-\phi) \Sigma'_2 \mathbf{R}_y^T(-\phi) \\ \Sigma_3 &= \mathbf{R}_x(\phi) \Sigma'_3 \mathbf{R}_x^T(\phi) \\ \Sigma_4 &= \mathbf{R}_y(\phi) \Sigma'_4 \mathbf{R}_y^T(\phi) \end{aligned} \quad (46)$$

where $\mathbf{R}_x(\phi)$ and $\mathbf{R}_y(\phi)$ are rotations of ϕ radians about the x - and y -axis, respectively. These definitions of the covariances were chosen arbitrarily to test (38), and do not correspond to any known real-world scenarios.

The results for configurations A , B , and D , shown in Fig. 3, demonstrate excellent agreement between the simulated

TRE_{rms} and (38). We computed the 95% confidence intervals of TRE_{rms} using the BC_a bootstrap method [37] with 1000 bootstrap replications. The value predicted by the square root of (38) was always within the confidence interval except for the smallest value of $d = 5 \text{ mm}$ where the marker configurations approached that of a straight line. This effect can be seen in the results for configuration B , and even more dramatically in the results for configuration C , which are shown in Fig. 4. Several interesting observations can be made from Fig. 4. First, for the noise covariances that we used, the HEIV algorithm produced only slightly smaller values of TRE_{rms} compared to Horn's method. Second, the HEIV algorithm produced worse results than Horn's method for values of $d < 50 \text{ mm}$; however, both methods were unreliable for values of d in this range. Third, the stiffness model overestimated TRE_{rms} at the smallest values of d when compared to Horn's method; this occurred because as the marker configuration approaches that of a line, one of the principal rotational stiffnesses approaches zero, which causes the TRE_{rms} predicted by (38) to grow rapidly.

The results for configurations A , B , and D showed that the optimal HEIV algorithm produced TRE_{rms} values between 0%–20% smaller than the values produced using Horn's method. We would like to note that the absolute TRE_{rms} values were less than 1 mm for values of $d > 50 \text{ mm}$; thus, the absolute improvement in TRE_{rms} was small for the fiducial marker configurations we examined. Of course, moving the target location farther away from the center of the fiducial markers would increase the absolute value of TRE_{rms} , and the potential improvement of using the optimal HEIV algorithm may become significant under these circumstances.

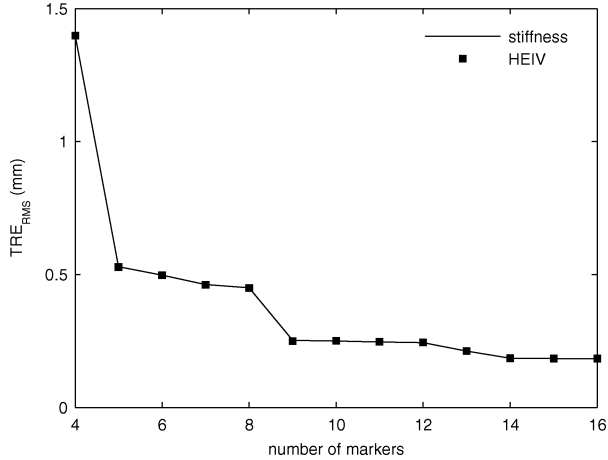


Fig. 5. Simulated and predicted TRE_{rms} values versus the number of fiducial markers.

B. Heteroscedastic Noise and Number of Markers

We validated (38) as a function of the number of markers by performing a simulation similar to the one used in the previous section. We formed a set of 16 fiducial markers by concatenating the markers from configurations D , C , B , and A using arc lengths of $d = 35, 30, 25$, and 25 mm respectively for each configuration; the different arc lengths were needed to prevent coincident markers. The markers were located on a sphere of radius 50 mm. We used the noise covariances defined by (44)–(46). The target location was $\mathbf{r} = [50 \ 50 \ 50]^T$.

The results are shown in Fig. 5. The results for (38) and the simulated values of TRE_{rms} agree to within better than 0.002 mm or 0.7% of the value obtained using (38); all results were contained within the 95% confidence interval for the mean of the simulated values.

C. Anisotropic Fiducial Localization Noise

Consider an optical tracking system and a calibrated digitizing stylus like the one shown in Fig. 6. The size of a typical CRF attached to a stylus used in computer-aided surgery is small compared to the dimensions of the working volume of the tracking system. It seems reasonable to assume approximately identically distributed FLE over all of the markers, as long as the markers on the CRF are identical and face the same direction. We choose to model FLE as a zero-mean, anisotropic Gaussian variable with the largest component being in the viewing direction of the camera. We also assume that FLE is independent of the orientation of the CRF relative to the camera. Note that this assumption is probably not realistic, and was made to illustrate how the behavior of TRE changes when the orientation of the CRF changes.

Suppose that a stylus oriented at 0° has its $z_s = 0$ plane perpendicular to the viewing direction of the optical tracker (i.e., directly facing the tracker). In our simulations, we rotated the stylus about its x_s -axis from -45° to 45° in increments of 7.5° . At each angle of rotation, we generated 10 000 sets of measured marker locations for the CRF. Each measured marker location \mathbf{m}_j was the model marker location \mathbf{p}_j rotated by the angle of rotation and contaminated with zero-mean, additive Gaussian

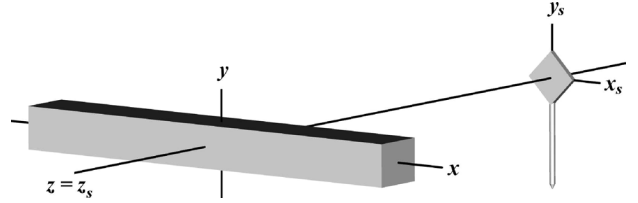


Fig. 6. Optical tracking system and stylus orientation used in our simulations. Measurement noise variance in the viewing direction, $-z$, is typically greater than those in the xy -plane.

noise of covariance $\Sigma_j = \text{diag}(s_x^2, s_y^2, s_z^2)$ where $s_x = s_y$ (isotropic noise in the xy -plane), $s_z = c s_x$ for some scalar $c \geq 1$ (anisotropic noise in the viewing direction), and $s_x^2 + s_y^2 + s_z^2 = S$ for a constant value $S = (0.1^2 + 0.1^2 + 0.3^2)$ mm² (constant total noise magnitude). All noise variances were given in the tracking camera coordinate system. The model marker locations were registered to the noisy measured marker locations using Horn's method, the HEIV method, and a slightly modified version of an unscented Kalman filter (UKF) algorithm [38]. For each registration, we computed TRE using the tip of the stylus as the target. At each angle, we computed the predicted TRE_{rms} using (38).

The UKF algorithm, as it was originally described, does not reliably converge to an accurate solution when using small numbers of markers [38]. To briefly review, the algorithm starts with the identity transformation as its registration estimate. It then processes the registration points sequentially using an unscented Kalman filter. Unlike an ordinary filter, it repeatedly processes the same registration points; i.e., the filter processes the first registration point, then the first two registration points, and so on, until the final iteration where all N registration points are processed. The convergence problem for small numbers of points can easily be remedied by allowing the algorithm to reprocess the final set of N registration points a few times; for our simulations, we reprocessed the final set of points twice.

1) *Stiffness Model Results:* The first set of simulations used the planar CRF shown in Fig. 7; planar configurations are currently the most common type of CRF used in commercial computer-aided surgical systems.

The second set of simulations were performed using a nonplanar CRF. The CRF had four markers in an irregular tetrahedral arrangement and was modeled on a commercially available CRF (VersaTrax TT002 series, Traxtal Technologies, Toronto, ON, Canada).

We observed significant differences in TRE_{rms} behavior between the planar and nonplanar CRFs. To verify these results, we modified the nonplanar Traxtal CRF to a planar CRF by moving the fiducial marker originally located at $[0, 0, 33]^T$ to $[0, 0, 0]^T$ and performed a third set of simulations.

The results for TRE_{rms} obtained using the HEIV and UKF algorithms, and the values predicted using (38) are shown in Fig. 8. We computed the confidence intervals of the mean of TRE_{rms} obtained using the HEIV and UKF algorithms. The curves produced using (38) passed through most of the confidence intervals. The maximum deviation between TRE_{rms} obtained using HEIV and that predicted by (38) was 0.009 mm,

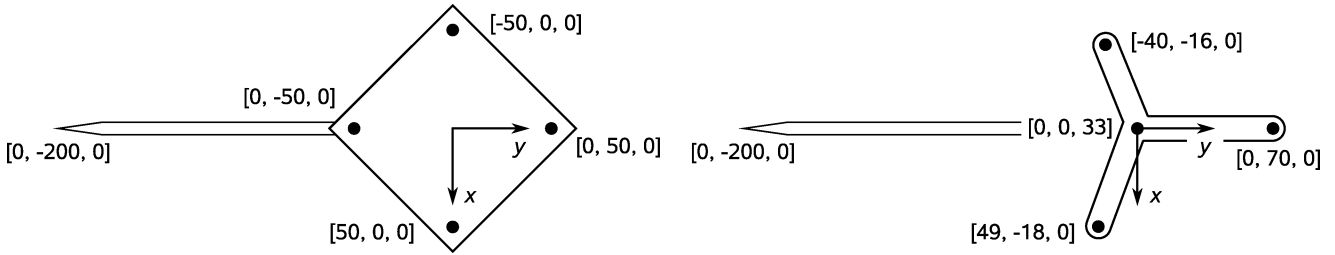


Fig. 7. Planar CRF (left) and nonplanar Traxtal CRF (right) stylus configurations.

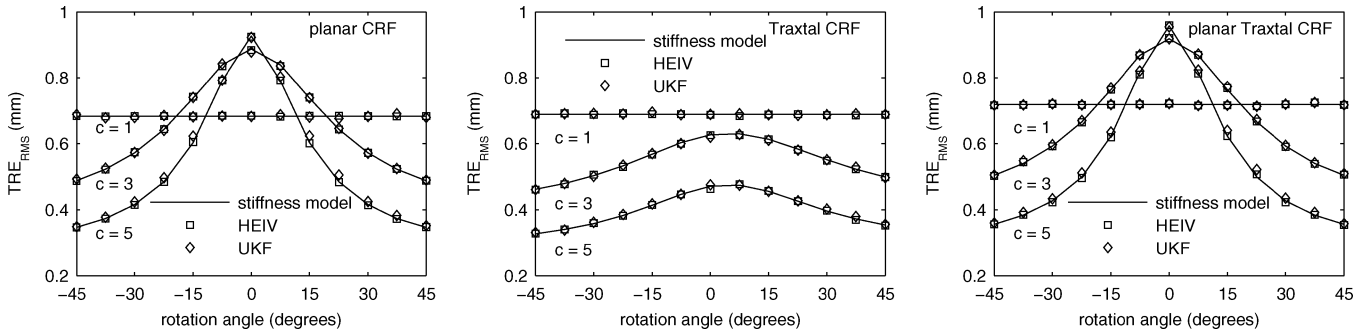


Fig. 8. TRE_{rms} predicted using (38) and TRE_{rms} obtained from simulations using HEIV and UKF registration algorithms for various levels of noise anisotropy. Shown from left to right are results for the planar, nonplanar Traxtal, and planar modified Traxtal CRF.

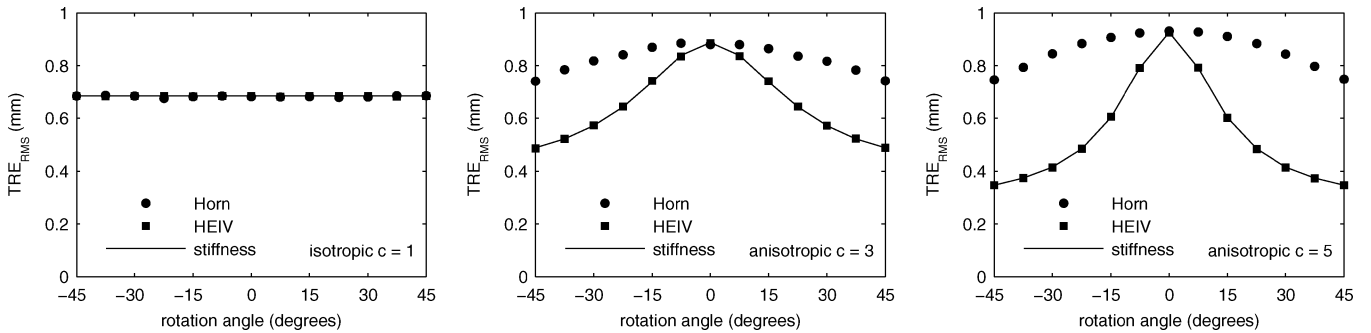


Fig. 9. TRE_{rms} predicted using (38) and TRE_{rms} obtained from simulations using Horn’s method and the HEIV algorithm for the planar CRF. Noise anisotropy increases from left to right.

which was 1.8% of the predicted value. The maximum deviation between TRE_{rms} obtained using the UKF algorithm and that predicted by (38) was 0.022 mm, which was 3.1% of the predicted value.

The isotropic noise TRE_{rms} can be predicted using (42) or (43). The predicted values for the planar, nonplanar Traxtal, and planar modified Traxtal CRF were 0.684, 0.688, and 0.7181 mm, respectively. These values were inside the simulation confidence intervals.

We observed a strong dependence on rotation angle for TRE_{rms} under anisotropic noise with the planar CRFs. The TRE_{rms} values actually exceeded the isotropic values for rotation angles around 0° , even though the total noise magnitude was the same for the isotropic and anisotropic cases. The nonplanar Traxtal CRF produced substantially less variation in TRE_{rms} as a function of rotation angle. The peak TRE_{rms} values under anisotropic noise occurred at 7.5° rotation but they did not exceed the isotropic value.

2) *Planar CRF Results:* The TRE_{rms} results are shown in Fig. 9. A peak occurred in the TRE_{rms} curves at 0° rotation as the fiducial localization noise became anisotropic. The peak was large when using HEIV, with TRE_{rms} changing by a factor as large as 2.67 between $\pm 45^\circ$ and 0° ($c = 5$). Horn’s method always produced the largest TRE_{rms} for a given rotation angle and the TRE_{rms} was always larger than the isotropic case. HEIV produced values of TRE_{rms} that were always smaller than Horn’s method except at 0° rotation. TRE_{rms} became smaller than the isotropic case as the rotation angle increased for HEIV.

We expected the rotational component of TRE_{rms} to dominate the total value because the tip of the stylus was far from the centroid of CRF. The mean absolute rotation error curves, shown in Fig. 10, had the same shape as the TRE_{rms} curves, agreeing with our expectations.

The standard deviations (in the three principal camera directions) of the tip location after registration are shown in Fig. 11. HEIV and Horn’s method had identical behavior under isotropic

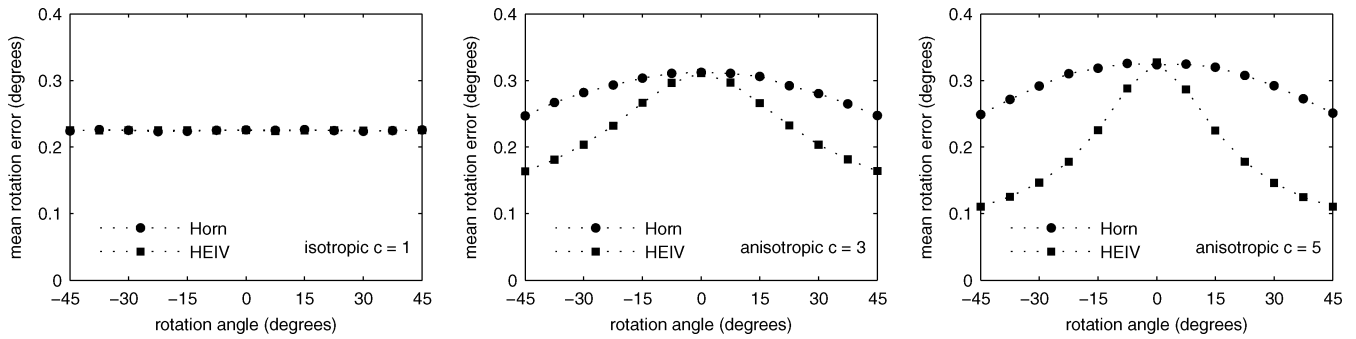


Fig. 10. Simulation results of mean absolute rotation error using Horn's method and the HEIV algorithm for the planar CRF. Noise anisotropy increases from left to right.

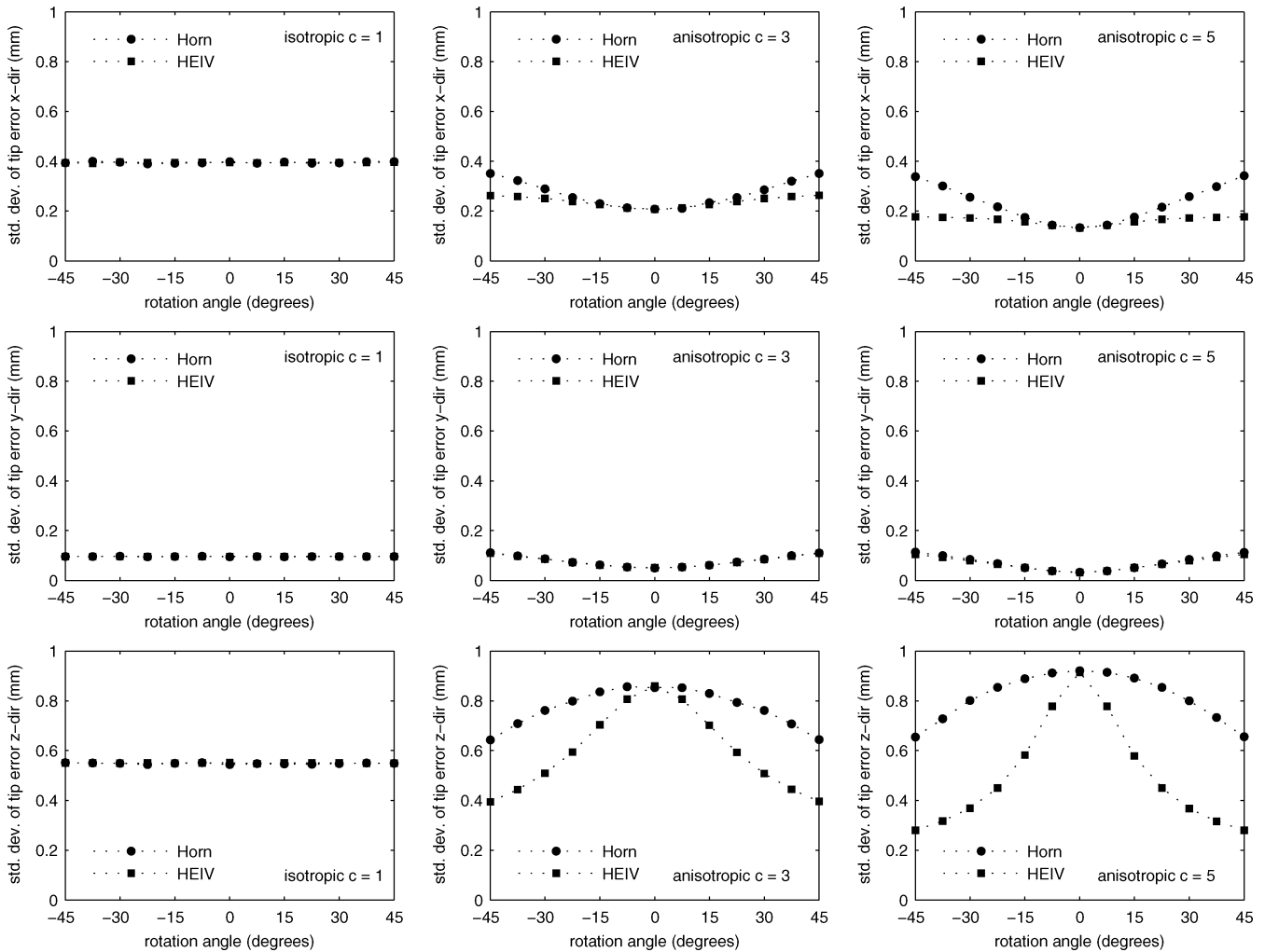


Fig. 11. Simulation results of tip error standard deviation using Horn's method and the HEIV algorithm for the planar CRF. Noise anisotropy increases from left to right, and the x , y , and z standard deviations are shown from top to bottom.

noise. Horn's method produced the largest standard deviations in the x - and z -directions under anisotropic noise.

3) *Nonplanar CRF Results:* The TRE_{rms} results are shown in Fig. 12. The TRE_{rms} values predicted using (38) closely matched the results obtained using the HEIV algorithm. The peak in the TRE_{rms} curves occurred at 7.5° rotation as the fiducial localization noise became anisotropic. The peak was much less pronounced compared to the planar CRF when using HEIV.

Horn's method always produced the largest TRE_{rms} for a given rotation angle and TRE_{rms} was always larger than the isotropic case. Unlike the planar CRF, TRE_{rms} produced using HEIV was smaller than that produced by Horn's method for all rotation angles. TRE_{rms} produced using HEIV with anisotropic noise was always smaller than that for isotropic noise.

The standard deviations of the stylus tip location after registration are shown in Fig. 13. HEIV and Horn's method had iden-

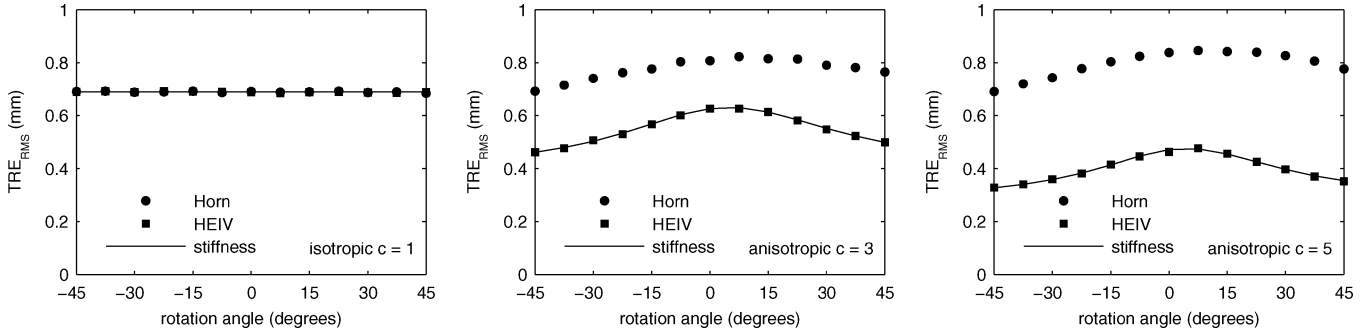


Fig. 12. TRE_{rms} predicted using (38) and TRE_{rms} obtained from simulations using Horn's method and the HEIV algorithm for the nonplanar Traxtal CRF. Noise anisotropy increases from left to right. nonplanar Traxtal CRF.

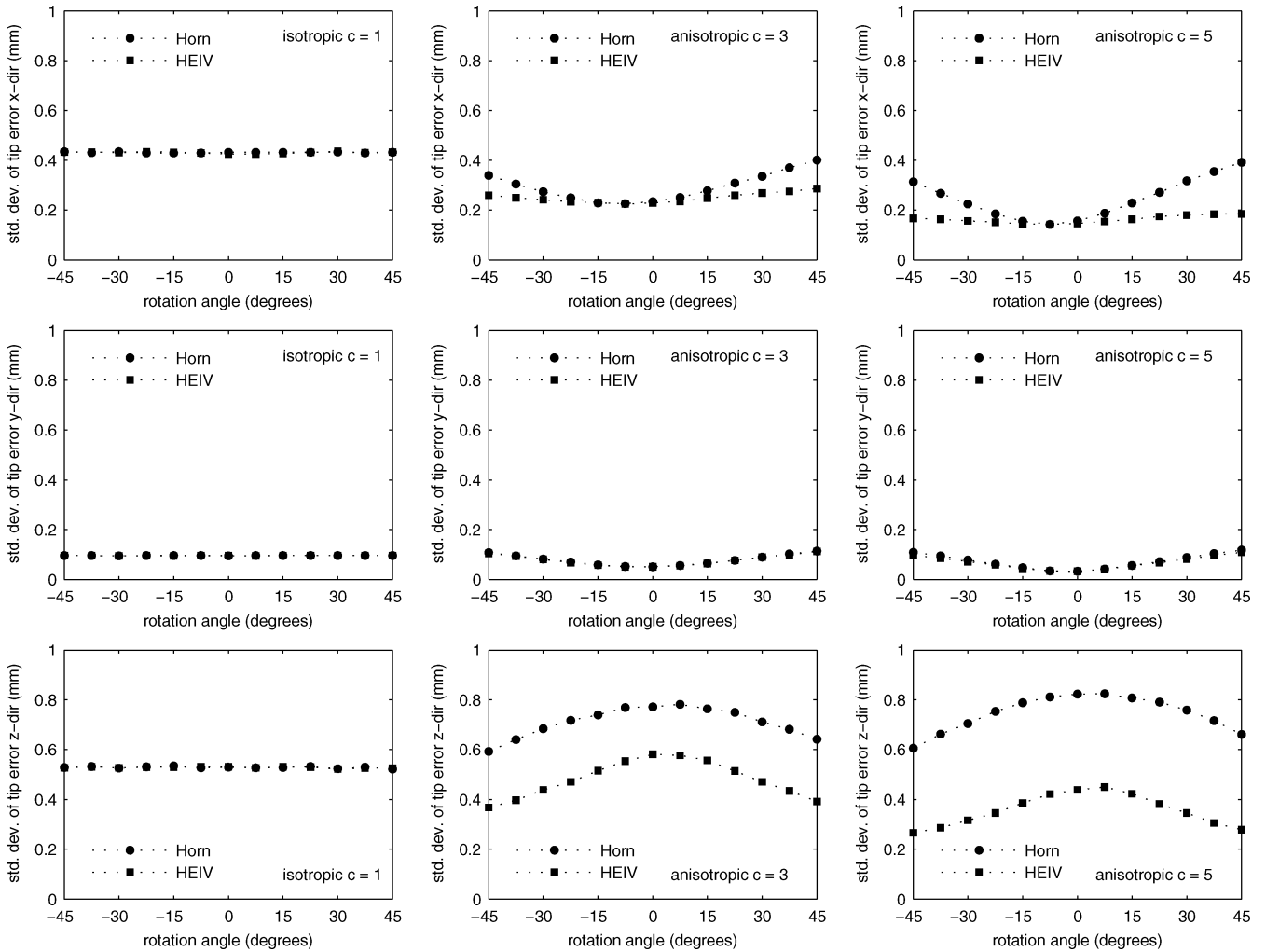


Fig. 13. Simulation results of tip error standard deviation using Horn's method and the HEIV algorithm for the nonplanar Traxtal CRF. Noise anisotropy increases from left to right, and the x , y , and z standard deviations are shown from top to bottom.

tical behavior under isotropic noise. Horn's method produced the largest standard deviations in the x - and z -directions under anisotropic noise.

4) *Planar CRF 2 Results:* The TRE_{rms} results, shown in Fig. 14, were similar to the first planar CRF, thus confirming that nonplanar CRF configurations lead to superior TRE behavior when there is anisotropic noise. The TRE_{rms} values predicted

using (38) closely matched the results obtained using the HEIV algorithm.

D. Sensitivity to Noise Covariance

The HEIV algorithm requires that the noise covariance be specified (up to a scalar constant). Although the FLE noise covariance can be estimated through laboratory experiments, there

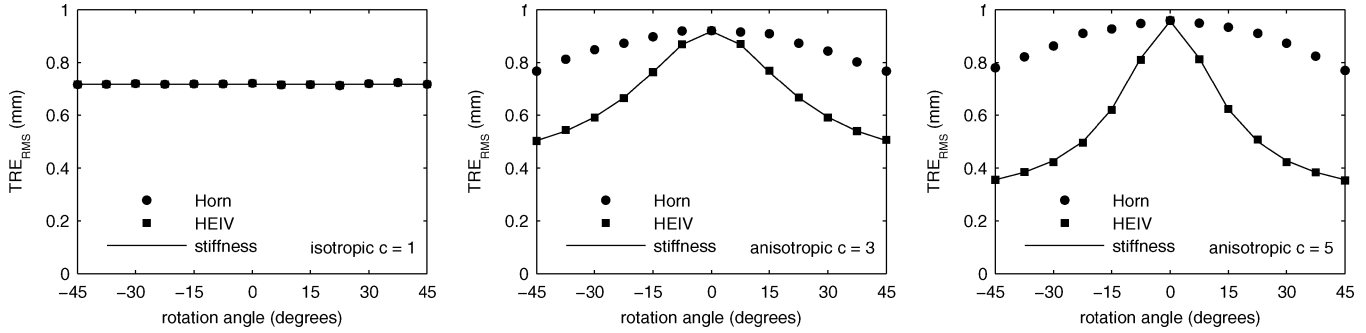


Fig. 14. TRE_{RMS} predicted using (38) and TRE_{RMS} obtained from simulations using Horn's method and the HEIV algorithm for the planar modified-Traxtal CRF. Noise anisotropy increases from left to right.

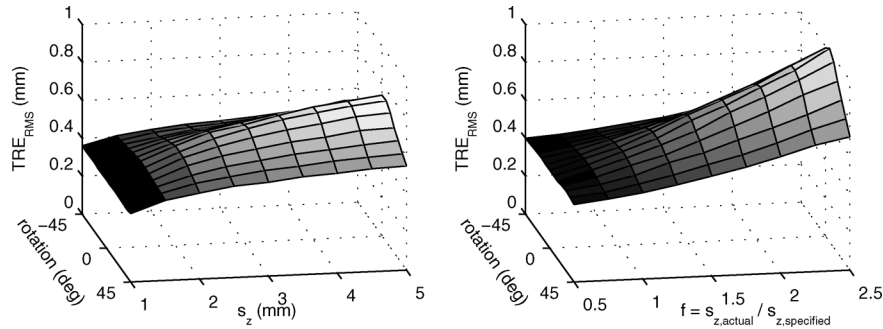


Fig. 15. Sensitivity of TRE_{RMS} to noise covariance for HEIV algorithm. (Left) Optimal results with matched specified and actual noise covariances. (Right) Results with fixed specified noise covariance and varying actual noise covariance.

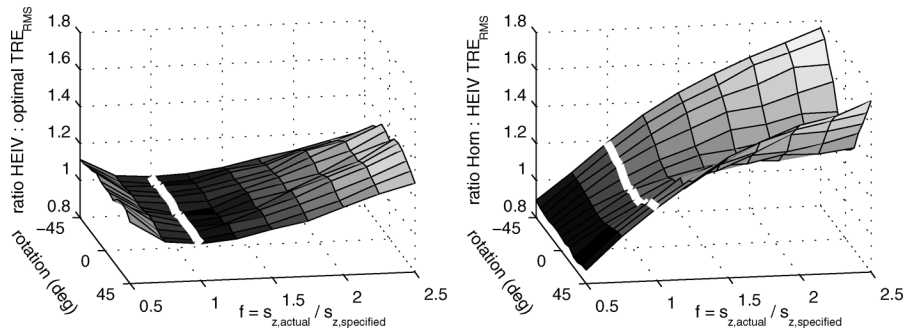


Fig. 16. Sensitivity of TRE_{RMS} to noise covariance for HEIV algorithm (Left) Ratio of TRE_{RMS} obtained using incorrectly specified noise covariance to optimal TRE_{RMS} . (Right) Ratio of TRE_{RMS} obtained using Horn's method to TRE_{RMS} obtained using HEIV with incorrectly specified noise covariance. The white curve at $f = 1$ are the results for correctly specified noise covariance.

remains the possibility that the specified noise covariance does not exactly match the true noise covariance; in such cases, it would be desirable that the HEIV algorithm perform no worse than the least-squares solution. We investigated the sensitivity of the HEIV algorithm to variations in the true noise covariance by fixing the specified noise covariance and changing the z -component of the actual noise covariance. Our simulations used the nonplanar Traxtal CRF. The specified noise covariance was defined as $\Sigma = \text{diag}(s_x^2, s_y^2, s_z^2)$ where $s_x = s_y = 0.1$ mm and $s_z = 0.2$ mm. The actual noise covariance used in the simulations was the same as the specified covariance except that s_z was varied as $s_z = 0.1, 0.15, \dots, 0.5$ mm. We examined our results as a function of the scalar ratio $f = s_{z,actual} / s_{z,specified}$.

The optimal TRE_{RMS} values, obtained by matching the specified and actual noise covariances, are shown in Fig. 15 along with the TRE_{RMS} obtained using unmatched covariances. As

expected, TRE_{RMS} obtained using unmatched covariances were larger than the optimal values. The disparity between matched and unmatched TRE_{RMS} values appeared to increase as the error between the specified and actual noise covariance increased.

The results for incorrectly specified noise covariance can be further clarified by computing the ratio of the optimal TRE_{RMS} value to the TRE_{RMS} value obtained using the specified noise covariance; this ratio is shown in Fig. 16. We observed between 11%–22% increase in TRE_{RMS} when the z -component of the noise covariance was overspecified ($f = 0.5$) or underspecified ($f = 2$) by a factor of two. These results suggest that the HEIV algorithm was not extremely sensitive to errors in specifying the viewing direction of noise covariance when using the nonplanar CRF.

It may be the case that Horn's method produces better estimates if the noise covariance is not exactly known. The ratio

of TRE_{rms} using Horn's method and HEIV with unmatched covariances is shown in Fig. 16. Horn's method almost always produced a TRE_{rms} greater than HEIV with incorrectly specified covariance. The exception occurred when the z -component of the noise covariance was overspecified by a factor of two.

V. DISCUSSION AND CONCLUSION

We were pleasantly surprised by the similarity between the values predicted by (38) and the simulated TRE_{rms} of the HEIV algorithm. The HEIV algorithm is known to be optimal under heteroscedastic Gaussian noise. Our simulations using fiducial configurations A – D with heteroscedastic noise showed that (38) reliably predicted TRE_{rms} except for near co-linear arrangements of markers; in these cases, (38) overestimated the value of TRE_{rms} . The simulations using the stylus CRFs produced a few instances where the predicted value of TRE_{rms} fell outside of the 95% confidence interval of the simulated value; however, the deviation from the value predicted using (38) was never more than 0.009 mm (1.8% of the predicted value) using HEIV, and 0.022 mm (3.1% of the predicted value) using the UKF algorithm. We believe that the differences were small enough that they can be attributed to natural variation in the Monte Carlo simulation results and do not suggest any serious flaw in our spatial stiffness model.

Our simulations using fiducial configurations A – D showed that a least-squares registration algorithm does not necessarily perform substantially worse than the optimal HEIV algorithm when there is heteroscedastic measurement noise. We observed between 0%–20% improvement in the simulation TRE_{rms} values when using the HEIV algorithm compared to Horn's method. Because (38) and (43) reliably predict TRE_{rms} we now have a way to computationally decide between using a least-squares and optimal algorithm.

We would like to emphasize that our simulations motivated by optical tracking assumed an FLE model that is too simplistic to model real tracking systems. These simulations were performed to illustrate the dependence of TRE on the orientation of a CRF relative to the noise covariances. Experiments using a tracked pointing stylus and an assumption of isotropic FLE have suggested that both infrared emitting diodes and retro-reflective spheres, when used as CRF markers, tend to produce an increase in TRE when the CRF is rotated away from the viewing direction of the tracking system [16]. The increase in TRE is believed to be caused by the markers not behaving as point light sources [39], which causes the FLE noise to become a function of rotation angle. We have not attempted to measure the dependency of the distribution of FLE on rotation angle for a tracking system, nor are we aware of any published results; lacking physical measurements, we did not attempt to model these affects in our simulations. The measurement and modeling of FLE is a possible area of future research.

We observed significant differences in TRE_{rms} between the least-squares and optimal registration algorithms when rotating the CRF during the tracking system simulations. Horn's method and the HEIV algorithm had identical worst performances when the CRF of the stylus was directly or almost directly facing the tracking camera (rotation angle around 0°). This result is

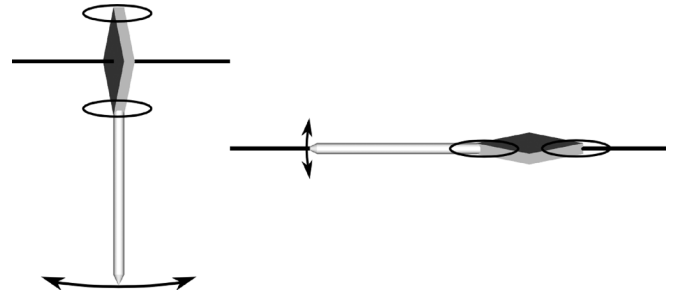


Fig. 17. (Left) Tip TRE is worst when the stylus is oriented to face the direction of greatest noise anisotropy (typically the viewing direction of the camera) because such an orientation results in the greatest expected rotational error. (Right) TRE is minimized by orienting the stylus face away from the camera viewing direction which minimizes the contribution of the rotational error.

easily explained with reference to Fig. 17. Suppose the CRF is directly facing the tracking system (left side of Fig. 17) and we rotate the CRF towards or away from the tracking system cameras. A small rotation about an axis parallel to the x -axis passing through the center of the CRF will cause the noise-free top and bottom markers to move predominantly in the z -direction. Conversely, measurement noise predominantly in the z -direction will induce a rotation parallel to the x -axis about the center of the CRF; such a rotation is magnified into a stylus tip TRE proportional to the length of the stylus. Because the magnitude of the rotation is determined almost completely by the largest noise component, the expected TRE is maximized in this orientation. Note that the measurement noise may also induce a rotation about an axis parallel to the y -axis, but such a rotation does not cause the tip of the stylus to be displaced; rotation about an axis parallel to the z -axis are minimized because the measurement noise is smallest in the x and y -directions. Suppose the CRF is rotated through 90° so that it faces perpendicular to the tracking camera (right side of Fig. 17). In this case, the rotational errors are determined primarily by the smallest measurement noises (those in the x and y -directions), and the tip TRE due to rotational error is minimized. Of course, in this situation, the CRF would likely be invisible to the tracking system.

Horn's method, which assumes isotropic noise, always produced the largest TRE_{rms} values in our simulations using anisotropic noise. The variances in the stylus tip location after registration were also largest for Horn's method. The HEIV algorithm produced lower TRE_{rms} values compared to Horn's method even when the noise covariances were incorrectly specified, except when the covariance was overspecified by a factor of two. Our results suggest that conservatively underestimating the anisotropic component of the noise covariance could safely produce a reduction in stylus tip TRE_{rms} .

West and Maurer [16] showed that a regular tetrahedron was the ideal configuration of fiducials for isotropic noise. Our results showed that a nonplanar configuration was also preferred over a flat CRF if there was identical anisotropic noise and an optimal registration algorithm is used. The nonplanar CRF produced only modest amounts of variation in TRE as a function of rotation angle. This was in sharp contrast compared to the planar CRF configurations that produced pronounced peaks in TRE_{rms} at 0° rotation. We observed that Horn's method, while producing higher values of TRE_{rms} , produced

only modest amounts of variation in TRE as a function of rotation angle regardless of the CRF configuration. We observed no significant advantages for the nonplanar CRF when Horn's method was used.

We have studied the case where a registration algorithm is used to match a model of a CRF to the measurements made by a tracking system. This approach is appropriate if the tracking system can measure the CRF fiducials simultaneously or if the velocity of the CRF is small; otherwise, motion artifacts will be present in the measured fiducial locations. An alternative method is to use a Kalman-type filter to perform the tracking, which removes the need for an explicit registration algorithm. One such filtering approach has been demonstrated that is capable of updating the pose of a CRF whenever a single fiducial location is measured [40], [41].

Two solutions for estimating TRE_{rms} under anisotropic noise were recently described by Wiles *et al.* [14] and Moghari and Abolmaesumi [15]. Those approaches were superior to ours in some respects; most significantly, they were able to derive the covariance of TRE. Our approach only estimates TRE_{rms} , but it does so without assuming a suboptimal, least-squares registration solution. Furthermore, the spatial stiffness analysis gives the individual contributions of the three translational and three rotational components of TRE. Lin *et al.* [27] used the stiffnesses as a quality measure for robotic grasps; similarly, the stiffnesses could be used as a quality measure for fiducial marker configurations. We believe that our analysis can be extended to surface-based registration, much like we did for the isotropic noise case [23].

The covariance propagation approach described by Sielhorst *et al.* [17], [18] produces the TRE covariance under heteroscedastic noise. We are investigating if their approach yields an identical estimate of TRE as ours; this study might yield some insight to determine TRE covariance from a stiffness approach.

We have previously described a spatial stiffness model for surface-based registration TRE under the assumption of identical, isotropic, zero-mean Gaussian noise [23]. We believe that the surface-based registration model can be extended to the case of heteroscedastic noise in a similar method to that described in this article. Validating such a model would require a registration algorithm capable of accommodating heteroscedastic noise in the registration points [42].

In summary, we have presented a spatial stiffness model of fiducial TRE under anisotropic noise, and we have validated the model using simulations with optimal registration algorithms. Our results suggest that a significant decrease in TRE_{rms} is possible if optimal algorithms are used in the presence of anisotropic noise, and if the noise covariances are approximately known.

REFERENCES

- [1] J. M. Selig, "Three problems in robotics," *Proc. Inst. Mech. Eng. Part C: J. Mech. Eng. Sci.*, vol. 216, no. 1, pp. 73–80, 2002.
- [2] J. M. Fitzpatrick, J. B. West, and C. R. Maurer Jr., "Predicting error in rigid-body point-based registration," *IEEE Trans. Med. Imag.*, vol. 17, no. 5, pp. 694–702, Oct. 1998.
- [3] K. S. Arun, T. S. Huang, and S. D. Blostein, "Least-squares fitting of two 3-D point sets," *IEEE Trans. Pattern Anal. Mach. Intell.*, vol. 9, no. 5, pp. 698–700, Sep. 1987.
- [4] B. K. P. Horn, "Closed-form solution of absolute orientation using unit quaternions," *J. Opt. Soc. Am. A*, vol. 4, pp. 629–642, 1987.
- [5] R. Khadem, C. C. Yeh, M. Sadeghi-Tehrani, M. R. Bax, J. A. Johnson, J. N. Welch, E. P. Wilkinson, and R. Shahidi, "Comparative tracking error analysis of five different optical tracking systems," *Comput. Aided Surg.*, vol. 5, pp. 98–107, 2000.
- [6] N. Ohta and K. Kanatani, "Optimal estimation of three-dimensional rotation and reliability evaluation," *IEICE Trans. Inform. Syst.*, vol. E82-D, no. 11, pp. 1247–1252, 1998.
- [7] B. Matei, "Heteroscedastic errors-in-variables models in computer vision," Ph.D. dissertation, Rutgers Univ., New Brunswick, NJ, 2001.
- [8] B. Matei and P. Meer, "Optimal rigid motion estimation and performance evaluation with bootstrap," in *Comput. Vis. Pattern Recognit.*: IEEE, 1999, pp. 339–345.
- [9] X. Pennec and J. P. Thirion, "A framework for uncertainty and validation of 3D registration methods based on points and frames," *Int. J. Comput. Vis.*, vol. 25, no. 3, pp. 203–229, 1997.
- [10] M. H. Moghari and P. Abolmaesumi, "A high-order solution for the distribution of TRE in rigid-body point-based registration," in *Proc. Med. Image Comput. Computer-Assisted Intervent. (MICCAI 2006)*, Copenhagen, Denmark, Oct. 2006, pp. 603–700.
- [11] M. H. Moghari and P. Abolmaesumi, "Comparing the unscented and extended Kalman filter algorithms in the rigid-body point-based registration," in *Proc. 28th Annu. Int. Conf. IEEE EMB*, 2006, pp. 497–500.
- [12] L. Dorst, "First order error propagation of the procrustes method for 3D attitude estimation," *IEEE Trans. Pattern Anal. Mach. Intell.*, vol. 27, no. 2, pp. 221–229, Feb. 2005.
- [13] J. M. Fitzpatrick and J. B. West, "The distribution of target registration error in rigid-body point-based registration," *IEEE Trans. Med. Imag.*, vol. 20, no. 9, pp. 917–927, Sep. 2001.
- [14] A. D. Wiles, A. Likholyot, D. D. Frantz, and T. M. Peters, "A statistical model for point-based target registration error with anisotropic fiducial localizer error," *IEEE Trans. Med. Imag.*, vol. 27, no. 3, pp. 378–390, Mar. 2008.
- [15] M. H. Moghari and P. Abolmaesumi, "Maximum likelihood estimation of the distribution of target registration error," *IEEE Trans. Med. Imag.*, 2009, to be published.
- [16] J. B. West and C. R. Maurer, Jr., "Designing optically tracked instruments for image-guided surgery," *IEEE Trans. Med. Imag.*, vol. 23, no. 5, pp. 533–545, May 2004.
- [17] M. Bauer, M. Schlegel, D. Pustka, N. Navab, and G. Klinker, "Predicting and estimating the accuracy of n-ocular optical tracking systems," in *Proc. 5th IEEE/ACM Int. Symp. Mixed Augmented Reality (ISMAR 2006)*, Oct. 2006, pp. 43–51.
- [18] T. Sielhorst, M. Bauer, O. Wenisch, G. Klinker, and N. Navab, "Online estimation of the target registration error for n-ocular optical tracking systems," in *Med. Image Computing Computer-Assisted Intervent. (MICCAI 2007)*, Brisbane, Australia, Oct. 2007, pp. 652–659.
- [19] W. Hoff and T. Vincent, "Analysis of head pose accuracy in augmented reality," *IEEE Trans. Vis. Comput. Graphics*, vol. 6, no. 4, pp. 319–334, 2000.
- [20] B. Ma and R. E. Ellis, "A spatial-stiffness analysis of fiducial registration accuracy," in *Proc. Med. Image Computing Computer-Assisted Intervent. (MICCAI 2003)*, Montreal, QC, Canada, Nov. 2003, pp. 359–366.
- [21] B. Ma and R. E. Ellis, "Spatial-stiffness analysis of surface-based registration," in *Proc. Med. Image Computing Computer-Assisted Intervent. (MICCAI 2004)*, Rennes/Saint-Malo, France, Sep. 2004, pp. 623–630.
- [22] B. Ma and R. E. Ellis, "A point selection algorithm based on spatial stiffness analysis of rigid registration," *Comput. Aided Surg.*, vol. 10, no. 4, pp. 1–15, 2005.
- [23] B. Ma and R. E. Ellis, "Analytic expressions for fiducial and surface target registration error," in *Proc. Med. Image Computing Computer-Assisted Intervent. (MICCAI 2006)*, Brisbane, Australia, Oct. 2006, pp. 637–644.
- [24] S. Huang and J. M. Schimmels, "The bounds and realization of spatial stiffness achieved with simple springs connected in parallel," *IEEE Trans. Robot. Autom.*, vol. 14, no. 3, pp. 466–475, Jun. 1998.
- [25] B. Ma, M. H. Moghari, R. E. Ellis, and P. Abolmaesumi, "On fiducial target registration error in the presence of anisotropic noise," in *Proc. Med. Image Computing Computer-Assisted Intervent. (MICCAI 2007)*, 2007, pp. 628–635.

- [26] R. M. Murray, Z. Li, and S. S. Sastry, *A Mathematical Introduction to Robotic Manipulation*. Boca Raton, FL: CRC, 1994.
- [27] Q. Lin, J. Burdick, and E. Rimon, "A stiffness-based quality measure for compliant grasps and fixtures," *IEEE Trans. Robot. Autom.*, vol. 16, no. 6, pp. 675–688, Dec. 2000.
- [28] J. M. Selig and X. Ding, "Structure of the spatial stiffness matrix," *Int. J. Robot. Autom.*, vol. 17, no. 1, pp. 1–15, 2002.
- [29] J. Lončarić, "Normal forms of stiffness and compliance matrices," *IEEE Trans. Robot. Autom.*, vol. RA-3, no. 6, pp. 567–572, Dec. 1987.
- [30] R. G. Roberts, "A note on the normal form of a spatial stiffness matrix," *IEEE Trans. Robot. Autom.*, vol. 17, no. 6, pp. 968–972, Dec. 2001.
- [31] T. Patterson and H. Lipkin, "Structure of robot compliance," *ASME J. Mech. Design*, vol. 115, no. 3, pp. 576–580, Sep. 1993.
- [32] T. Patterson and H. Lipkin, "A classification of robot compliance," *ASME J. Mech. Design*, vol. 115, no. 3, pp. 581–584, Sep. 1993.
- [33] R. A. Horn and C. R. Johnson, *Matrix Analysis*. Cambridge, U.K.: Cambridge Univ. Press, 1985.
- [34] A. C. Rencher, *Methods of Multivariate Analysis*. New York: Wiley, 1995.
- [35] J. L. Meriam and L. G. Kraige, *Engineering Mechanics: Dynamics*. New York: Wiley, 1986.
- [36] C. R. Maurer, Jr., J. M. Fitzpatrick, M. Y. Wang, R. L. Galloway, Jr., R. J. Maciunas, and G. S. Allen, "Registration of head volume images using implantable fiducial markers," *IEEE Trans. Med. Imag.*, vol. 16, no. 4, pp. 447–462, Aug. 1997.
- [37] T. J. DiCiccio and B. Efron, "Bootstrap confidence intervals," *Stat. Sci.*, vol. 11, no. 2, pp. 189–228, 1996.
- [38] M. H. Moghari and P. Abolmaesumi, "Point-based rigid-body registration using an unscented kalman filter," *IEEE Trans. Med. Imag.*, vol. 26, no. 12, pp. 1708–1728, Dec. 2007.
- [39] Polaris Tool Design Guide 4th ed. Northern Digital Inc., 2007.
- [40] G. Welch, "SCAAT: Incremental tracking with incomplete information," Ph.D. dissertation, Univ. North Carolina, Chapel Hill, NC, 1996.
- [41] G. Welch and G. Bishop, "SCAAT: Incremental tracking with incomplete information," in *SIGGRAPH '97: Proc. 24th Annu. Conf. Comput. Graphics Interactive Tech.*, 1997, pp. 333–344.
- [42] R. S. J. Estépar, A. Brun, and C.-F. Westin, "Robust generalized total least squares iterative closest point registration," in *Proc. Med. Image Computing Computer-Assisted Intervent. (MICCAI 2004)*, Rennes/Saint-Malo, France, Sep. 2004, pp. 234–241.